Supplementary information

Nanoscale mechanics of antiferromagnetic domain walls

In the format provided by the
authors and unedited

Supplementary Information: Nanoscale mechanics of antiferromagnetic domain walls

Natascha Hedrich, Kai Wagner, Brendan J. Shields, and Patrick Maletinsky[*]

Department of Physics, University of Basel, Klingelbergstrasse 82, Basel CH-4056, Switzerland

Oleksandr V. Pylypovskyi, Tobias Kosub, and Denys Makarov

Helmholtz-Zentrum Dresden-Rossendorf e.V., Institute of Ion
Beam Physics and Materials Research, 01328 Dresden, Germany

Denis D. Sheka

Taras Shevchenko National University of Kyiv, 01601 Kyiv, Ukraine

[*] patrick.maletinsky@unibas.ch

I. POSITION CALIBRATION

As we are using open-loop piezo scanners (Attocube ANSxyz100), we need to calibrate their physical displacement and determine the piezo non-linearity in order to achieve accurate fitting of the domain wall. To do so, we perform atomic force microscopy (AFM) measurements of our sample's topography on a commercial system (Bruker Dimension 3100), and compare various length scales as offered by patterned mesas on the sample surface to those measured by our system. This allows us to determine the conversion factor from applied voltage (V) to physical piezo displacement (µm) for a wide range of piezo voltages as shown in Fig. S1a. Errors on individual points here are below the marker size. We integrate the fitting functions given in the legends to convert from our system coordinates (in voltage) to real coordinates (in µm) as shown in Fig. S1b. This leads a non-linear conversion, which corrects for deformations in our measurements (Fig. S1b, inset). We make this explicit by showing a 2D stray field image in Fig. S1c, where the original image (with scale in applied voltage) is shown in the top panel and the adjusted scaling conversion in the bottom panel. The difference between the two images is most apparent when one compares the visible curvature of the domain wall in both figures.
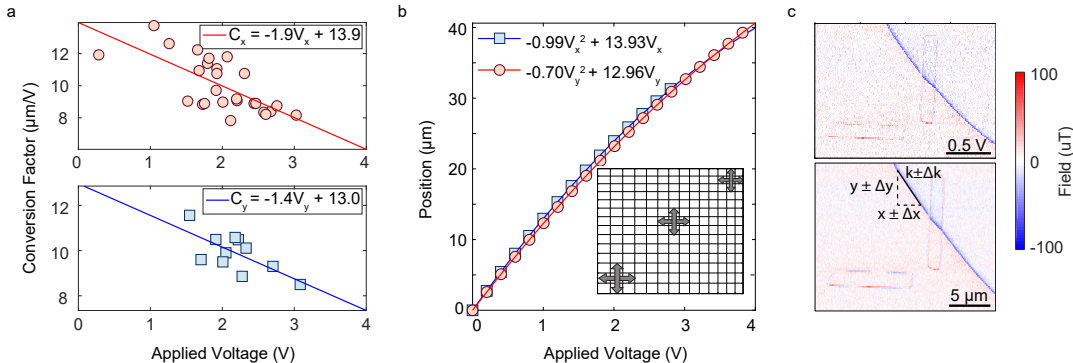

FIG. S1. **Calibration of the piezo position a** The conversion factor from applied voltage (V) to displacement (µm) as a function of the applied voltage for the x (top) and y (bottom) axes. **b** Plot of the position (as determined by integrating the conversion factor in **a**) as a function of the voltage applied in the x direction (blue squares) and y direction (red circles). The fit parameters are given in the top right inset. The bottom right inset shows the resulting deformation of equally spaced lines in a 2D plot, with dark gray arrows shown for emphasis. **c** Stray field image of two mesas together with the domain wall plotted with the position in applied voltage (top) and the converted position in µm (bottom).

II. DOMAIN WALL NUCLEATION AND MORPHOLOGY

As received, the single crystal Cr_2O_3 was in a mono-domain state, confirmed with high probability by measuring the same sign of the surface magnetization at number of mesas (see Section IV) across the surface of the crystal. The DW is then nucleated as described in the methods and using the device shown in Fig. S2a. We use the same method of sampling the magnetization across the sample to localize the DW. The nucleated DWs appear smooth and straight, as seen when imaging the domain wall over larger areas. The approximate orientation of the DW, as determined by NV magnetometry, is shown in Fig. S2b with cyan lines for subsequent nucleation procedures, separated by an erasure of the domain wall through electromagnetic cooling in a homogeneous field. Note that these positions differ from the nominal location of the split-gate gap (shown by a thick, white line), indicating that the domain wall is mobile during the nucleation process. Furthermore, upon annealing the sample at $\approx 453\,\mathrm{K}$, the domain wall position changed drastically, as shown in the right panel of Fig. S2b, where the initially nucleated position is shown with a dashed line, and the final position, after annealing is shown with a solid line. We would like to note that the observation that

a domain wall may persist even when heated above the Néel temperature is not a new one, and that this phenomenon was already explored by Brown in 1969 [1]. We also show an additional stray field image of the domain wall in Fig. S2c, taken at the bottom right of the cyan line shown in the inset. This emphasizes the fact that the domain wall, in the absence of mesa structures and strong pinning centers, is indeed smooth at the micrometer scale and suggests that the pinning we observe is primarily due to the interaction between mesa and DW. Further examples of this pinning are shown in the bottom two panels of Fig. S2c. In these two images, we observe simultaneous pinning at multiple mesa edges following both nucleated instances of the domain wall.
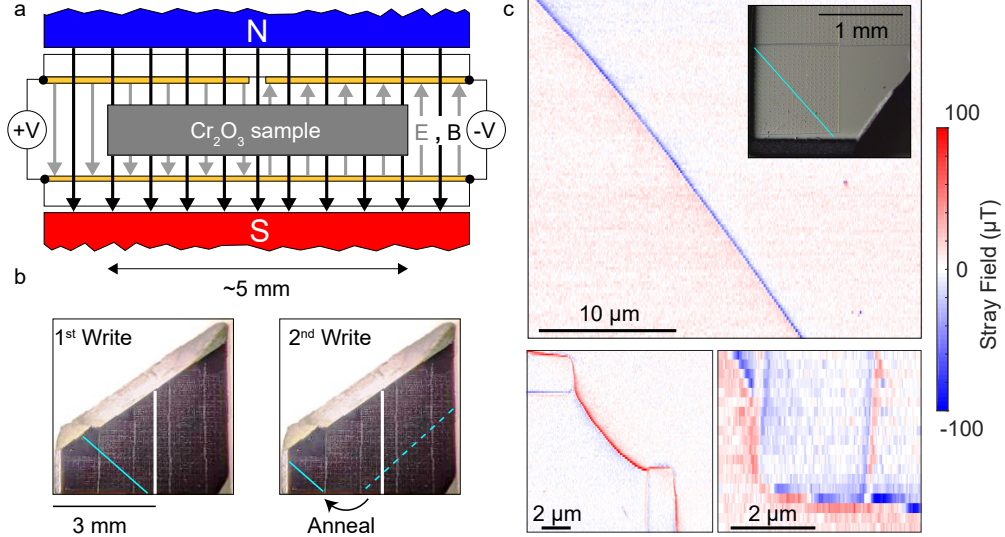

FIG. S2. **Nucleation of domain walls a** A schematic representation of the setup used to nucleate domain walls in a single crystal of Cr_2O_3. The north and south poles of the permanent magnets are shown with the field direction given by the black arrows. The grey arrows show the direction of the electric field, generated by applying voltages $\pm V$ between the top contacts and ground. **b** Optical images of the crystal with the approximate locations of the split-gate gap during nucleation shown with a thick, white line. The final domain wall position is given by the solid, cyan line. In the left image, the dashed cyan line shows the position of the domain wall before annealing. **c.** (top) Stray field image of the domain wall showing its general smoothness and straight orientation. The inset shows a microscope image of the domain wall position, shown by the solid, cyan line, with the area of the stray field scan taken at the bottom right end of the line. (bottom) Stray field images showing (left) simultaneous pinning at two different mesa edges after the first poling and (right) a further example of DW pinning to two edges of a mesa after the second poling.

III. METROPOLIS HASTINGS

We use a form of the Metropolis Hastings (MH) algorithm to infer the probability distributions of parameters in difficult-to-sample data sets [2, 3]. This MH-based parameter estimation is chosen, since the model involves correlated parameters and exhibits many local good fits to the data. Such conditions make it difficult for gradient descent methods to determine a global minimum in the difference between the data and the model as typically characterized by the mean squared error (MSE). Additionally, the analysis via the MH algorithm allows us to better estimate the uncertainty on the involved parameters by combining several datasets. For all analyses of the magnetic and sensor properties (parameters p) discussed in the main text, we evaluate the recorded stray field (data D) with a theoretical description (model) using the following implementation of this iterative algorithm (with n steps):

1. A set of initial starting parameters (p_{curr}), a step size (d_i) for each parameter and a theoretical model

3

are defined.

2. A second new candidate set of parameters p_{new} is drawn from a proposal distribution. For this, a symmetric normal distribution is used, which is centered around the current values p_{curr} with a width $= 2d_i$, which realizes a random-walk MH algorithm to find the next candidate parameters.

3. The model function is then computed for both parameter sets and compared with the measured data D to estimate the two likelihoods r_{curr} and r_{new}, of the data, given p_{curr} or p_{new}, respectively. We assume unbiased Gaussian noise on the data and Jeffreys priors on the variance [3]. In particular, the likelihood is evaluated as $r_{\text{new/curr}} \propto (R+1)^{-(\nu+1)/2} \approx R^{-(\nu+1)/2}$, where $\nu = |D| - |p_{\text{new/curr}}|$ ($|\cdot|$ is the size of the set) and R is the MSE of our model given the data and model parameters. Often additional prior knowledge is available on certain parameters (e.g. as a restriction to bounds or normal distributions based on previous data), in which case, we multiply these to r following the Bayesian rule for the posterior. The probability for accepting p_{new} is then realized following the typical iterative operational implementation:

   - Select a random value a, uniformly distributed between 1 and 0.
   - **If** $(r_{\textbf{new}}/r_{\textbf{curr}}) \leq a$: Accept the new parameters p_{new} and set $p_{\text{curr}} = p_{\text{new}}$.
   - **Else:** Keep the parameter set p_{curr}.
   - Draw a new candidate set based on p_{curr}.
   - Repeat this procedure n times.

We apply this analysis to both the mesa and domain wall stray fields using the model functions and data acquisition described in the following sections.

A typical evolution of a single parameter normalized to its starting value is shown in Fig. S3 as a function of the iteration number. In the initial period, the parameters evolve towards the region of a better model representation of the data (higher likelihood) before it settles to a stochastic walk around a particular value (thermalization). The iteration steps before reaching this point are dropped when later examining the distribution of values, and are referred to as the "burn-in region" [2, 3]. The remaining steps are then processed into histograms for each parameter value, obtaining a marginalized and unnormalized probability distribution for each parameter. We test for an underlying correlation of the steps by only considering every η^{th} value (thinning). In the last step, the distribution curves are approximated by Gaussians to estimate a mean and a standard deviation for a given parameter based on the data and model used.
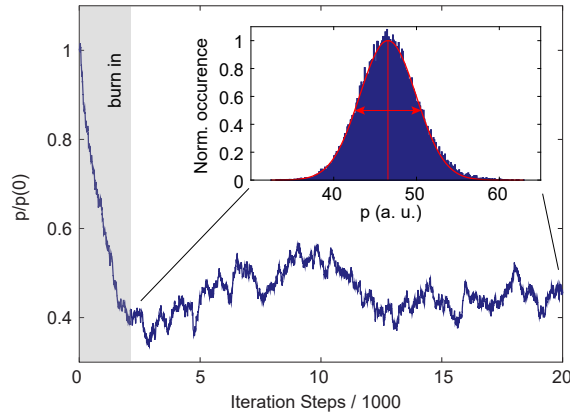

FIG. S3. **Typical single parameter evolution in the Metropolis Hastings algorithm** The parameter values relative to its starting value as a function of the iteration steps of the algorithm. The initial burn-in period is shown by the shaded area. The inset shows the histogram of values taken after the burn-in period, fitted with a Gaussian distribution, with the mean and FWHM shown with red bars.

4

IV. MESA STRAY FIELDS

In order to extract quantitative magnetic and sensor information from a mesa, we record its stray field while scanning the magnetometer in a line that crosses the mesa (linecut). This data is then compared to a well-established model [4] for the stray field of a magnetic stripe, where the field arises from effective currents (I_+, I_-) running along the top and bottom of its edges as shown in Fig. S4a. According to this model, the stray field measured at a distance d_{NV} from a single edge of a mesa, oriented along the y-axis, is given by:

$$B_{NV} = \sin(\theta_{NV})\cos(\phi_{NV})B_x + \sin(\theta_{NV})\sin(\phi_{NV})B_y + \cos(\theta_{NV})B_z, \tag{S1}$$

$$B_x = \frac{-\mu_0\sigma_m}{2\pi}\left(\frac{d_{NV}}{(x-x_0)^2+d_{NV}^2} - \frac{(d_{NV}+t)}{(x-x_0)^2+(d_{NV}+t)^2}\right), \text{ and} \tag{S2}$$

$$B_z = \frac{\mu_0\sigma_m}{2\pi}\left(\frac{x-x_0}{(x-x_0)^2+d_{NV}^2} - \frac{x-x_0}{(x-x_0)^2+(d_{NV}+t)^2}\right). \tag{S3}$$

Here, σ_m is the magnetization, t is the thickness of the mesa, x_0 is the location of the edge, θ_{NV} and ϕ_{NV} are the polar and azimuthal angles of the NV axis respectively and $\mu_0 = 4\pi \times 10^{-7}$ N/A^2 is the vacuum permeability. Note that $B_y = 0$ in this configuration. These equations describe the stray fields (B_x and B_z) on one side of the mesa, and as such, we add the corresponding terms for the second edge (located at x_1). In order to take into account a possible asymmetric tip shape or accumulation of dirt during scanning, we allow for two different NV distances (d_{NV} and $d_{NV} + \Delta d$) for either side of the mesa, as described in [5].

With this particular analytical form, we now address the recorded stray field data and are left with seven fitting parameters ($\sigma_m, d_{NV}, \theta_{NV}, \phi_{NV}, x_0, x_1, \Delta d$). In the first step we seek to infer the sensor orientation (θ_{NV},ϕ_{NV}), since we can assume it to be constant throughout all measurements. For this, we perform an initial least-squared fit, seeded from 50 different initial parameter sets and choose the best fit parameters. These parameters, together with the measured stray field values and model described above (Eq. S1), are then used to initialize the MH algorithm (see Section III). From all the combined datasets (29 individual linecuts), we infer the likelihood-distribution of the sensor orientation, by multiplying the individual likelihood distributions of the sensor-angles from each dataset. The resulting distribution is then described by a Gaussian, yielding a θ_{NV} and ϕ_{NV} of 60.7 ± 2.9 deg and 260.6 ± 0.8 deg respectively.

While there is no reason for θ_{NV} and ϕ_{NV} to vary between scans, we can not assume the remaining parameters to stay constant throughout all datasets. Therefore, we proceed with the analysis of individual linescans, with the global sensor orientation as prior knowledge. The 29 individual parameter sets are iterated until the resulting (unnormalized) probability distributions are smooth ($n \approx 5 \times 10^6$ iterations) and approximate them by Gaussians. Note that here, we need to account for the position error arising from the open-loop scanner as described in Section I. This is done by calibrating our length scale and the statements on the error of the individual parameters.

An example of this analysis for the data set in Fig. S4b is shown in Fig. S4(c,d). We approximate each of these histograms with a Gaussian and extract its mean and the standard deviation. For this particular data set, we extract $\sigma_m = 2.4 \pm 0.2$ μ_B/nm^2, $d_{NV,0} = 46 \pm 3$ nm and $d_{NV,1} := \Delta d + d_{NV,0} = 53 \pm 3$ nm (not shown). In the main text, we state the mean of σ_m obtained at room temperature together with the systematic error.

V. DOMAIN WALL MODEL

In order to derive a model for the stray field of a domain wall, we consider the surface magnetization of Cr$_2$O$_3$. As for the mesa measurements (Section IV), in our experiments the emerging stray field B_{NV} is measured along the NV axis:

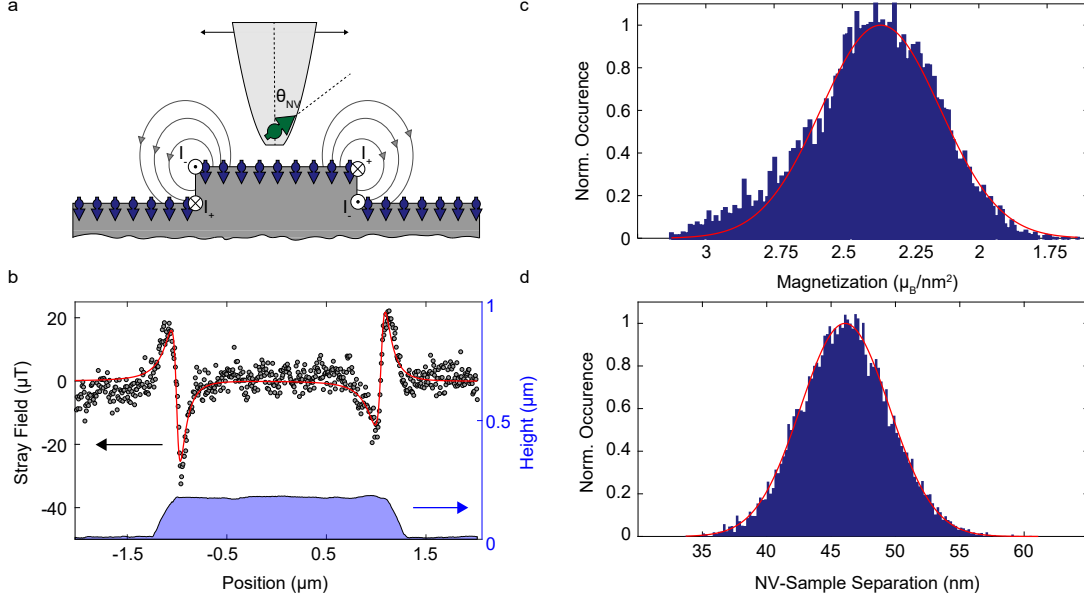$$B_{NV} = B_0 + \cos(\theta_{NV})B_z + \cos(\phi_{NV})\sin(\theta_{NV})B_x, \tag{S4}$$

5

FIG. S4. **Fitting of the mesa stray field a** Schematic of a mesa with the surface magnetization shown as an array of oriented spins. The stray field lines are shown in grey, originating from effective currents, I_+ and I_-, at the edges of the mesas. The NV is located at the tip of the scanning probe, which is scanned relative to the mesa. **b** Stray field of the mesa as measured along the NV axis with the fit of the model shown in red. The topography of the stripe is shown at the bottom. **c,d** Histograms of the results of the MH algorithm for the surface magnetization (c) and NV-to-sample spacing, $d_{NV,0}$ (d). These are fit with Gaussian distributions (shown in red) and the mean and standard deviation for each distribution is given in the text.

To calculate this field, we use the procedure of propagating fields in Fourier space (with momentum vector q) [6], where for a given magnetization $M(q)$, the Fourier components of the magnetic strayfield for a given sensor distance d_{NV} can be calculated with the corresponding propagator $D(q, d)$:

$$B(q, d_{NV}) = D(q, d_{NV})M(q),\tag{S5}$$

with:

$$D(q, d) = \frac{\mu_0 M_s}{2}(e^{-dq} - e^{-(d+t_m)q}) \begin{bmatrix} -\cos^2(\phi_q) & -\frac{\sin(2\phi_q)}{2} & -i\cos(\phi_q) \\ -\frac{\sin(2\phi_q)}{2} & -\sin^2(\phi_q) & -i\sin(\phi_q) \\ -i\cos(\phi_q) & -i\sin(\phi_q) & 1 \end{bmatrix}.\tag{S6}$$

Here, t_m is the thickness of the magnetic layer and M_s [μA/m] is the saturation magnetization. For the two-dimensional surface magnetization, we consider the limiting case $t_m \cdot q \ll 1$ such that, $\sigma_m = M_s \cdot t_m$ is the surface magnetization, and the exponential pre-factor simplifies to $\frac{\mu_0 \sigma_m q}{2}(e^{-dq})$.

After an inverse Fourier transformation, one obtains the real-space x and z components of the stray field of a Bloch wall:

$$B_x = -\frac{\mu_0 \sigma_m}{2\pi^2 \ell_m} \text{Re}\left[-\psi^{(1)}\left(\frac{2d_{NV} + \pi\ell_m + 2ix}{2\pi\ell_m}\right) + \psi^{(1)}\left(\frac{2d_{NV} + \pi\ell_m - 2ix}{2\pi\ell_m}\right)\right],\tag{S7}$$

$$B_z = \frac{\mu_0 \sigma_m}{2\pi^2 \ell_m} \text{Im}\left[-\psi^{(1)}\left(\frac{2d_{NV} + \pi\ell_m + 2ix}{2\pi\ell_m}\right) + \psi^{(1)}\left(\frac{2d_{NV} + \pi\ell_m - 2ix}{2\pi\ell_m}\right)\right].\tag{S8}$$

6

Here, $\psi^{(1)}$ represents the first derivative of the log gamma function. Note that the situation is translation invariant along the y-direction, and therefore produces no stray field in B_y.

In order to validate this analytical description of the stray field of a domain wall, we simulate a Bloch wall in MuMax3 [7]. In the simulation, the surface magnetization of Cr_2O_3 is approximated by a thin slab given by a single cell with a 1 nm extent and a magnetization M of $|M| = 10$ kA/m , exchange stiffness $\mathcal{A} = 0.423$ pJ/m and uniaxial anisotropy of $K = 215.86$ J/m^3. The total dimensions of the simulated sheet are 4096 nm $\times$ 32 nm $\times$ 1 nm discretized to a grid of 1 nm $\times$ 2 nm $\times$ 1 nm cells, including periodic boundary conditions to minimize boundary artifacts.

To nucleate a domain wall, we start by considering a sheet magnetized upwards in one half and downwards in the other. After energy minimization of the system via relaxation, a time-span of about 1 μs is simulated to ensure a static equilibrium. The magnetization profile of the domain wall is then extracted and fitted according to the wall profile described by Eq. (1-3) in the Methods, which yields ℓ_m. In the next step, the stray field at a distance of 20 nm is extracted from the simulation and compared with Eq. S8. We find very good agreement between the numerical estimates and analytical approximations. In fact, we believe the analytical description to be more accurate in capturing the dipolar stray fields, since the model considers an infinitely extended magnetic system, without the need of periodic boundary conditions or finite extent as present in the simulations. Such a comparison is shown in Fig. S5.
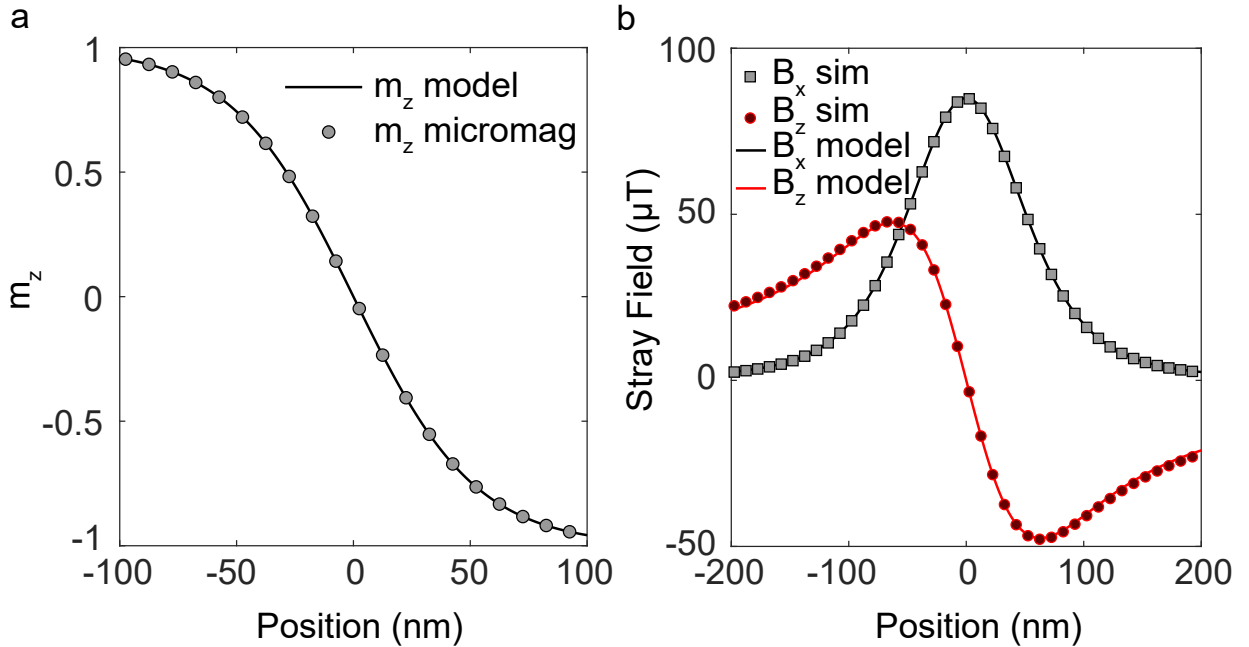

FIG. S5. **a** Normalized magnetization profile of a Bloch domain wall obtained from micromagnetic simulations (black dots) and its analytical description (solid line). **b** Stray field components B_x, B_z (black square, red dots) simulated for a 20 nm distance from the sample surface and calculated stray fields according to the analytical model (lines). For better visibility in both sub-panels, only every 10th data point of the simulation is shown.

VI. DOMAIN WALL FITTING

Based on concurrent measurements taken over the mesa structures, we can place tight restrictions on the values of σ_m, θ_{NV}, ϕ_{NV} and d_{NV}. In particular, for d_{NV}, we use the estimate for the larger of the two extracted distances $(d_{NV,0}, d_{NV,1}$, see Section IV) to account for possible dirt when scanning. The scanning direction with respect to our NV axis is readily obtained through our position calibration (Section I), though

again, taking into account the error on the angle. This leaves only the domain wall position and magnetic length ℓ_m as complete unknowns.

To proceed, the stray field data of the domain wall, prior information and stray field model (as derived in Section V) is analyzed via our MH algorithm implementation (Section III). We iterate through $n \approx 20 \times 10^6$ steps, resulting in a reasonable modeling of the recorded stray field data, as shown in Fig. S6b and smooth probability distributions for all parameters, in particular for the remaining magnetic length (ℓ_m) that determines the width of the domain wall.

The inset of Fig. S6b shows the cumulative distribution function (CDF) of ℓ_m for this data set. The measurement is taken at $302\,\mathrm{K}$, and yields a mean magnetic length of $20\,\mathrm{nm}$ with the 2nd and 98th percentiles being $2\,\mathrm{nm}$ and $28\,\mathrm{nm}$ respectively.

We claim that statements on such small ℓ_m ($\ell_m \ll d_{NV}$) parameters are still reasonable due to the immediate lateral and temporal proximity of the mesa and domain wall measurements. This allows us to assign any broadening in the stray field of the DW, exceeding the expected broadening from the sensor distance d_{NV}, to the domain wall width given by ℓ_m. This is essentially a deconvolution of the domain wall data with the detection function of our setup, possible by the concurrently taken mesa measurement data. The analysis yields our statistical confidence in the model parameters given in the data. In our experience, most systematic errors can be excluded, with the exception of the error arising due to the piezo non-linearity, drift and hysteresis characterized in Section I. We consider the possibilities of these errors in our statement of the DW upper bound by referring to the 98th percentile, while remaining within a reasonable range of values.
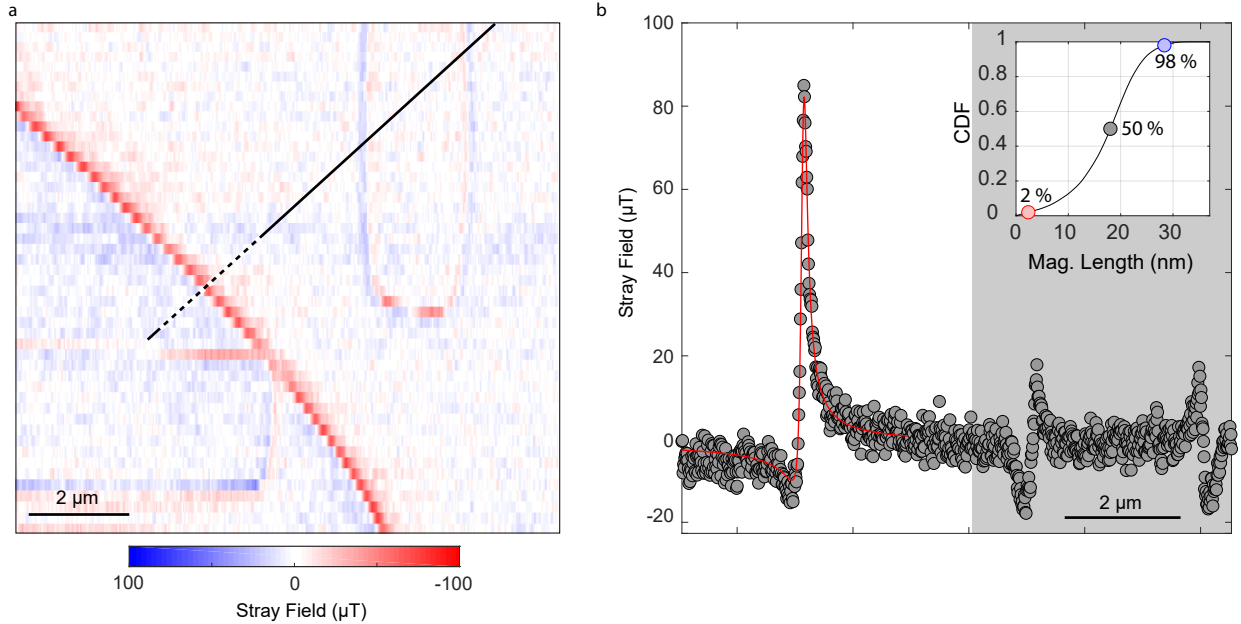

FIG. S6. **Fitting of the domain wall a** Full field image of the domain wall running between two perpendicular mesas. The black line shows the location of the linescan, with the domain wall portion given by the dashed line. **b** The stray field over the entirety of the linecut showing the domain wall fitted with the MH algorithm (red) and the mesa stray field in the grey area. The inset shows the CDF of the distribution of magnetic lengths with the 2%, 50% and 98% points shown with colored circles.

VII. TEMPERATURE DEPENDENCE

By mounting the sample on a small Peltier element, we are able to access a range of sample temperatures from room temperature (295.7 K) up to ≈340 K. As such, we are able to explore the temperature dependence of both the sample magnetization and ℓ_m. We begin by presenting the magnetization, extracted as described
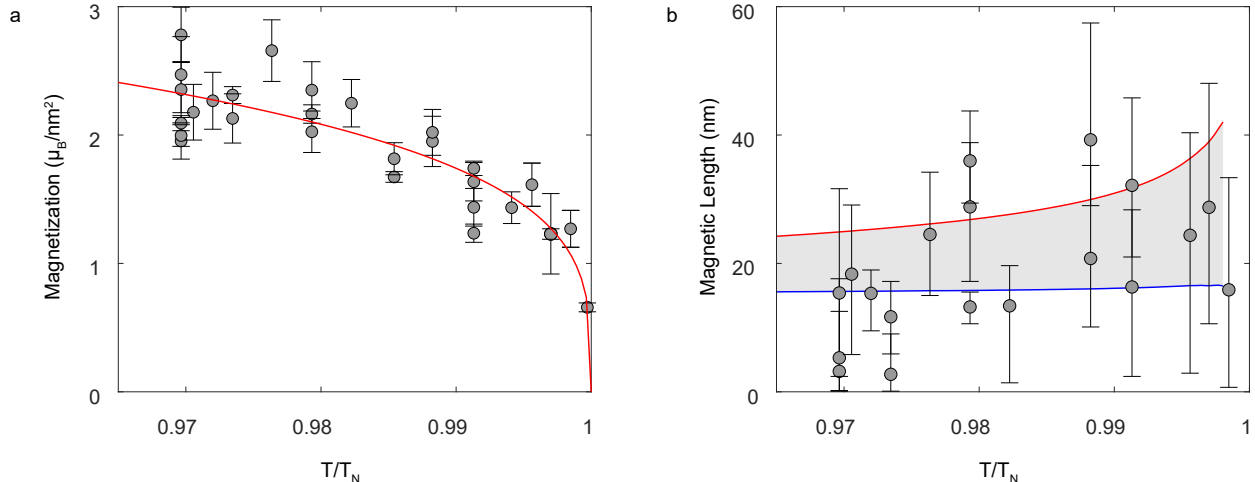

FIG. S7. **Temperature dependence of σ_m and ℓ_m a** The surface magnetization, as extracted from the mesa fits, plotted as a function of temperature. The error bars in the magnetization are given by the standard deviation of the extracted magnetization distributions (see Section IV). The fit is given by Eq. S9 for $T_{\text{Néel}} = 307$K. **b** The magnetic length (ℓ_m) is plotted as a function of temperature, with the mean DW parameter given by the circular points. The upper and lower limits, shown with black bars, are determined by the 98% and 2% confidence intervals respectively. The range of theoretical DW parameter values is presented by the shaded region between the red and blue lines. Note that all errors in the horizontal axis are smaller than the symbols.

in Section IV, and plotted against the temperature (normalized to the Néel temperature, $T_{\text{Néel}}$) in Fig. S7a. Here, we see that the surface magnetization falls off as

$$\sigma_m = \sigma_{m_0} \left(1 - \frac{T - T_0}{T_{\text{Néel}}} \right)^\beta, \tag{S9}$$

where β is the critical exponent. Note that we allow for an offset, T_0 of the temperature to take into account a possible calibration offset between the thermistor (which defines T) and the actual sample temperature. Here, we assume the literature value of the Néel temperature (307 K), a reasonable assumption in the absence of excessive strain [8] or doping [9], which may lead to changes in $T_{\text{Néel}}$. In doing so, we obtain a relatively small offset of only 2 K and a critical exponent $\beta = 0.26$, well within the range of previously measured values [10].

Note that the vertical error bars in Fig. S7a are given by the standard deviation of a Gaussian fit to the distribution of σ_m, extracted using the MH algorithm. We now repeat the same procedure for ℓ_m, plotted against the temperature in Fig. S7b. Here, the filled circles represent the mean magnetic length extracted from the MH algorithm for each data set. The error bars are given by the 98th (2nd) percentiles of the CDF, to show the maximum (minimum) values of ℓ_m that would be consistent with our data given the constraints we place based on the mesa measurements. In particular, we can look at the room temperature measurements (first three points at the left), which all fall below the 98th percentile bar at 32 nm. This justifies our statement in the main text, that $\ell_m > 32$ nm is inconsistent with our measurements at room temperature. Furthermore, we show the theoretical upper (blue) and lower (red) limits given by $\ell_m = \sqrt{\mathcal{A}/\mathcal{K}}$ where $\mathcal{A}$ is the exchange stiffness and $\mathcal{K}$ is the anisotropy [11]. In particular, we use the following temperature

dependence for $\mathcal{A}$ [12, 13]:

$$\mathcal{A}(T) = \mathcal{A}(0) \left[\frac{m(T)}{m(0)} \right]^\alpha, \tag{S10}$$

where m is the sublattice magnetization and $\alpha \in [1, 2]$. The exact value of α is unknown, but is believed to be close to $\alpha = 2$ yielding generally smaller domain wall widths. Furthermore, the value of $\mathcal{A}(0)$ is estimated as:

$$\mathcal{A}(0) = \frac{\mathcal{J}S^2}{a}, \tag{S11}$$

with the exchange integral $\mathcal{J} = 2.34 \times 10^{-21}$ J taken from DFT data [14] and $S = 1$ being the effective spin length [12]. As such, we see that our measurements are consistent with the theoretical expectations, and expect that, close to the Néel temperature, we would reach a regime where $\ell_m > d_{NV}$, in which case, we could directly measure ℓ_m. This would require either higher spatial resolution (for lower temperatures) or a higher sensitivity (close to $T_{\text{Néel}}$), which should be achievable in future work.

VIII. ANALYTICS FOR SNELL'S LAW

We consider a semi-infinite sample with a mesa of width w and thickness t on the top surface ($z = 0$). It is assumed that the mesa has a constant rectangular cross-section and is directed along the $\boldsymbol{e}_y$ axis. The continuum model of Cr_2O_3 can be represented using two antiferromagnetically coupled sublattices with unit magnetization vectors $\boldsymbol{M}_a(\boldsymbol{r})$ and $\boldsymbol{M}_b(\boldsymbol{r})$ [15, 16]. Within the long-wave approximation, it is reasonable to use the Néel vector order parameter $\boldsymbol{L}(\boldsymbol{r}) = (\boldsymbol{M}_a - \boldsymbol{M}_b)/2$ and the total magnetization vector $\boldsymbol{M}(\boldsymbol{r}) = (\boldsymbol{M}_a + \boldsymbol{M}_b)/2$, with $|\boldsymbol{L}| = 1$ and $|\boldsymbol{M}| \approx 0$. The latter will be neglected in the following. Then, the effective energy of the sample reads [17, 18]

$$\mathcal{E} = \mathcal{K} \int \left[\ell_m^2 \sum_{\nu=x,y,z} (\partial_\nu \boldsymbol{L})^2 + (1 - L_z^2) \right] d\boldsymbol{r}, \tag{S12}$$

where $\ell_m = \sqrt{\mathcal{A}/\mathcal{K}}$ is the magnetic length as for the spin-lattice model. Note that additional magnetoelastic terms may be incorporated into the effective value of the anisotropy constant $\mathcal{K}$, leading to a shift in ℓ_m with qualitatively identical results [19–21]. We furthermore assume the exchange-driven Neumann boundary conditions for the Néel vector:

$$\boldsymbol{L} \times (\mathbf{n}_\text{s} \cdot \nabla)\boldsymbol{L} = 0, \tag{S13}$$

where $\mathbf{n}_\text{s}$ is the surface normal. In the following, we use the local spherical reference frame parametrization $\boldsymbol{L} = \{\sin\vartheta \cos\varphi, \sin\vartheta \sin\varphi, \cos\vartheta\}$. We set the equilibrium, bulk domain wall position to the plane $y = kx$ where k is assumed to be small. We also assume a mesa geometry satisfying $t/w > 0.01$. Then, we can describe the domain wall as it passes through the mesa through the following Ansatz:

$$\vartheta = \begin{cases} 2\arctan\exp\frac{y'-y_0^\text{b}(x',z)}{\ell_m}, & z < 0 \\ 2\arctan\exp\frac{y-y_0^\text{m}(x,z)}{\ell_m}, & z \geq 0 \end{cases} \qquad \varphi = \text{const.} \tag{S14}$$

Here, $(x', y') = R_{\boldsymbol{e}_z}(\nu)(x, y)$ with $R_{\boldsymbol{e}_z}(\nu)$ being the rotation matrix around $\boldsymbol{e}_z$ at an angle ν, and $y_0^\text{b,m}$ describes the domain wall profile in bulk and mesa, respectively. We use

$$y_0^\text{b}(x, z) = (k_0 - k)b \operatorname{sech}\frac{x}{b} \tanh\frac{x}{b} e^{-\frac{z^2}{2c^2}} \tag{S15}$$

with $b = w/(2\operatorname{arcsinh} 1)$. The values of k_0 and c are determined through the energy minimization below. The function $y_0^\text{m}(x, z)$ is determined by minimizing the energy functional (S12) within the mesa and reads

$$y_0^\text{m}(x, z) = \frac{4k_0}{w} \sum_{n=0}^\infty \frac{(-1)^n}{\lambda_n^2} \operatorname{sech}\lambda_n t \cosh\lambda_n(t - z) \sin\lambda_n x, \tag{S16}$$

10

where $\lambda_n = \dfrac{(1 + 2n)\pi}{w}$ and we set $y_0^{\mathrm{m}}(x, 0) = k_0 x$. Then, the total energy of the domain wall ($\mathcal{E}$), up to a constant, reads:

$$\mathcal{E} = \mathcal{E}_0 k^2 w^2 \left[1 - f\left(\frac{t}{w} \right) \right], \quad f(x) = \left[C_2 + C_1 \sum_{n=1}^{N_0} \frac{\tanh \pi (2n - 1)x - 1}{(2n - 1)^3} \right]^{-1},$$

$$\mathcal{E}_0 = \frac{16 \mathcal{K} \ell_m}{\pi^3 C_1}, \quad C_1 = \frac{48 \sqrt{70} \arcsinh^2 1}{7 \pi^{7/2}} \approx 0.811, \quad C_2 = 1 + \frac{7}{8} \zeta(3) C_1 \approx 1.853,$$

(S17)

where $\zeta(3) \approx 1.202$ is the value of the Riemann zeta-function and N_0 is chosen from condition $\tanh \pi (2N_0 - 1)x \approx 1$. The value of c from Eq. (S15) is thereby given by $c = \sqrt{\dfrac{5}{14}} \dfrac{w}{2 \arcsinh 1}$. This parameter plays a particularly important role as it determines the length scale over which inhomogeneities in the domain wall persist into the bulk below the mesa. For this reason, we rename this parameter as t_B in the main text. Furthermore, $k_0 = k f(t/w)$ characterizes the direction of the domain wall at the bulk-mesa interface. Note, that it is dependent only on the mesa aspect ratio, which allows us to scale simulations for direct comparison with experiment. In particular, Fig. S8 shows the comparison between the analytics developed here (solid
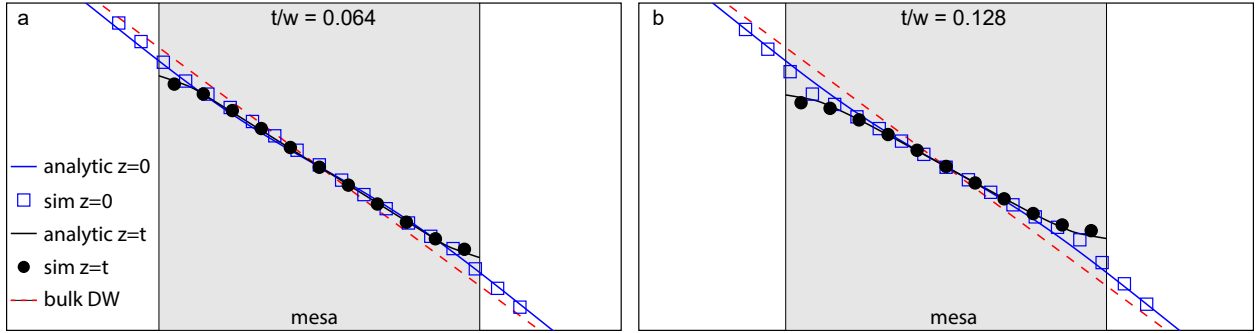

FIG. S8. **Analytical analysis of the domain wall in the bulk and mesa** Comparison of the domain wall profile in analytics (solid lines) and simulations (symbols) for two mesa aspect ratios. Level $z = t$ (top of mesa, see Eq. (S16)) and level $z = 0$ (bulk-mesa interface, see Eq. (S15)) are shown by black and blue. Equilibrium direction of the domain wall in bulk is shown by red dashed line. Mesa region is colored by gray. Simulation parameters: $w = 47a$, $t = 3a$ **a** and $t = 6a$ **b**, sample dimensions (without mesa) $199a \times 199a \times 49a$.

black and blue lines) and simulations (black circles and blue squares, where we see excellent agreement. In both analytics and simulation, we see the S-shaped bending of the domain wall on the mesa and the gradual twisting of the domain wall to match that of the bulk position (red dashed line) as we go into the bulk. The S-shaped deviation is much less pronounced for thinner mesas (Fig. S8a), which is very similar to the experimental case.

The Snell's law for the domain wall can be determined using the equilibrium domain wall profile in bulk and at the mesa top surface ($z = t$). The incidence angle is given by $\theta_1 = \arctan k$, while the refraction angle can be estimated as $\theta_2 = \arctan k_1$ with $k_1 := \partial_x y_0^{\mathrm{m}}(0, t)$. Then,

$$\frac{\sin \theta_1}{\sin \theta_2} = \frac{k}{k_1} \sqrt{\frac{1 + k_1^2}{1 + k^2}} \overset{t/w \to 0}{\approx} 1 + 3.1 \cos^2 \theta_1 \frac{t}{w}.$$

(S18)

IX. ELASTIC PROPERTIES OF THE DOMAIN WALL

In experiments and simulations, we have observed a behavior of the DW that mimics that of a rubber band. As such, we describe the DW trajectory and interactions with the mesa using its elastic properties,
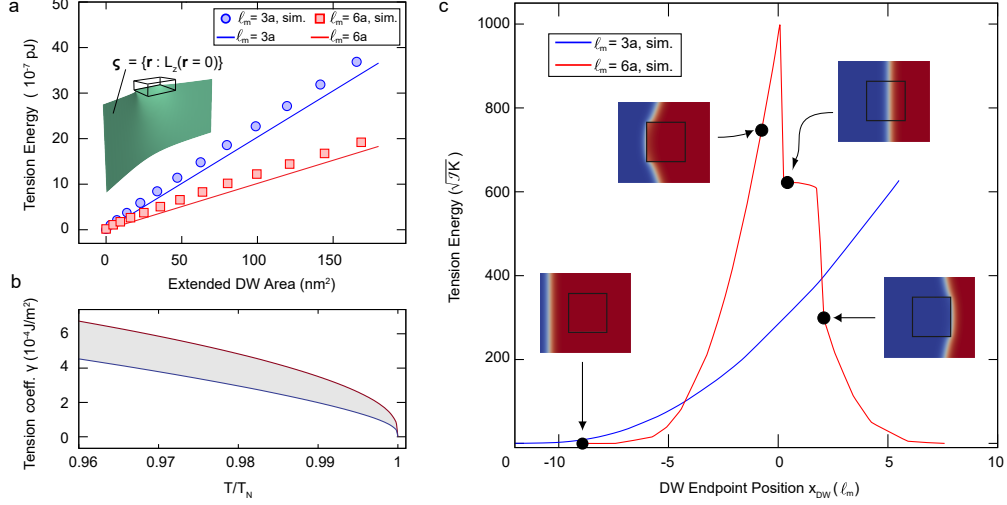
FIG. S9. **Extended simulations on DW elasticity a** Surface energy of the DW as a function of the increased DW area arising due to a bend around a mesa. We compare simulations (circles and squares) and calculations (lines) for two different magnetic length values $\ell_m = 3a$ (blue) and $\ell_m = 6a$ (red) **b** Temperature dependence of γ showing upper and lower bounds determined as in Fig. S7, showing the softening of the DW elasticity with increasing temperatures. **c** Pinning behavior of the DW for two effective temperatures (set by changing the magnetic length), where the blue curve ($\ell_m = 3a$) is at a lower temperature than the red ($\ell_m = 6a$). The insets show snapshots of the simulated DW position along the red curve. The blue curve corresponds to that seen in Fig. 3c in the main text.

that is, the DW surface energy and corresponding surface tension. In particular, we can consider the surface ς where the Néel order parameter lies horizontally ($L_z(\boldsymbol{r}) = 0$), and use this to describe the DW. We can address the details of ς by means of spin lattice simulations (see Simulation Details in the main text for more details). In Fig. 2c of the main text, we see that the domain experiences the strongest deflection at the edge of the mesa when crossing from bulk to mesa. As previously discussed, this behavior is well-described by the Ansatz in Eq. S14, where the b parameter determines how far the wall is deflected in the plane of the mesa and c (introduced in Eq. S15) characterizes the deflection in the vertical direction. The same behavior exists in the case where the domain wall is deformed around the mesa, as shown in the inset of Fig. S9a. Here, ς exhibits a smooth bend deep in the bulk and sharper deflections near the mesa edges. The additional, tensional energy due to this bending is plotted here for two different values of ℓ_m (circles and squares) as a function of the increase in area DW area $\mathcal{S}$ arising from the bending. We can compare the results of these simulations with analytical calculations if we assume that the inhomogeneities of ς are gradual, i.e. have a radius of curvature larger than ℓ_m. In this case, we can describe the DW's mechanical tension by:

$$\gamma = \mathcal{E}/\mathcal{S} = 4\sqrt{\mathcal{A}\mathcal{K}}. \tag{S19}$$

Here, we have defined a tension coefficient γ for the DW, which is plotted in Fig. S9a as solid lines for two different values of ℓ_m.

We can furthermore explore the impact of temperature on the tension coefficient. To do so, we use the temperature dependence of $\mathcal{A}$ [12, 13] and $\mathcal{K}$ [11], as in Fig. S7b. The corresponding upper and lower bounds of the tension coefficient are then shown in as shown in Fig. S9b, where the observed reduction in γ with increasing temperature implies an increase in elasticity, or a 'DW softening'. The consequences of this are more clear in Fig. S9c. Here, we show the pinning surface (tension) energy of the domain wall as a function of the DW position relative to a mesa, as in Fig. 3c in the main text, for two different values of ℓ_m. As ℓ_m increases with increasing temperature, this acts as an effective tuning parameter for the temperature in these simulations. The blue curve is as shown in Fig. 3c, where the DW deforms continuously. However, for larger ℓ_m (red), i.e. higher temperatures, we see a different pinning behavior, illustrated with the snapshots inset to the figure. Here, the DW is first deformed around the mesa, before snapping into a straight configuration,

12

passing through the mesa. As the DW is moved closer to the opposite edge of the mesa, the mesa will again be preferentially pinned to the mesa edge for some distance, on the order of ℓ_m, at which point the DW no longer feels the influence of the mesa. Thus, we expect that the pinning of the DW can be strongly influenced by temperature. However, this reduction in pinning strength can be overcome by carefully tuning the mesa geometry.

X. DOMAIN WALL DRAGGING

We are able to explain dragging of the domain wall by the laser through the formation of an effective attractive potential for the DW by local heating. Heating of the sample appears to lower the effective depth of pinning potentials, evidenced by the fact that reproducible laser dragging is only achieved at sample temperatures above room temperature, and near $T_{\text{Néel}}$. The additional heating provided by the laser then allows us to completely overcome this barrier, and move the domain wall freely. However, once the heating, i.e. laser, is removed, the domain wall tension causes the wall to snap back to its original position unless it becomes pinned along the way. This dragging and pinning can also be achieved over μm-scale distances, as shown in Fig. S10a, where we drag the DW using the same technique outlined in the main text, over a distance of 6 μm. This implies that every time we observe a movement of the DW, we are moving it between strong pinning sites, which can be internal crystal defects or fabricated surface structures.
We support these claims by further scans across the domain wall with the NV scanning probe at increased laser intensities. In this way, we aim to heat the sample with the near-field of the excitation laser near the tip of the scanning probe while simultaneously measuring the stray field from the DW at the NV position. An example of this procedure is shown in Fig. S10b, where we compare the measured stray field at low power (9.7 μW - red) and high power (85 μW - blue) 532 nm laser excitation (with powers measured at the rear lens of the microscope objective). Each scan is performed with a 3 s integration time per point, over the same section of domain wall, at a global sample temperature of 304.5 K. At low power, we see a domain wall stray field as already discussed. Increasing the power results in additional peaks in B_{NV} occurring at erratic locations. We explain this observation with a number of pinning sites located along the DW path as the DW is bent by laser dragging. In particular, we see an initial increase and plateau in B_{NV}, which is consistent with an attractive potential moving the domain wall ahead of the NV position. The field then increases, meaning that we pass over the domain wall with the NV, which can only be achieved by pinning of the domain wall. However, at some point, the pinning is overcome and the domain wall is again dragged together with the laser. We furthermore see a number of smaller pinning centers, evidenced by the slight peaks in field towards the end of the scan. In the insets of Fig. S10b, we show the position of the NV relative to the stray field pattern that would result in such peaks. Furthermore, as we continue to observe a non-zero stray field while scanning, we expect that the sample temperature surrounding the NV is still below $T_{\text{Néel}}$. If we again image the domain wall at low green laser power after such dragging, we see that the position remains unchanged in most cases. This indicates that the other pinning centers we observed are rather weak, and are overcome by the domain wall tension. Thus, we can directly observe the dragging of the domain wall by the laser and thereby gain information about the pinning landscape in the sample - a potential avenue for future research.

[1] Brown, C. A. *Magnetoelectric domains in single crystal chromium oxide*. PhD thesis, Imperial College of Science and Technology, , Oct (1969).

[2] Robert, C. P. *The Metropolis-Hastings Algorithm*. Wiley Stats Ref: Statistics Reference Online, (2015).

[3] Bolstad, W. *Bayesian Statistics Using Conjugate Priors*. Wiley Online Library: Understanding Computational Bayesian Statistics, (2009).

[4] Tetienne, J.-P., Hingant, T., Martinez, L., Rohart, S., Thiaville, A., Diez, L. H., Garcia, K., Adam, J.-P., Kim, J.-V., Roch, J.-F., and et al. The nature of domain walls in ultrathin ferromagnets revealed by scanning nanomagnetometry. *Nature Communications* **6**, 6733, Apr (2015).
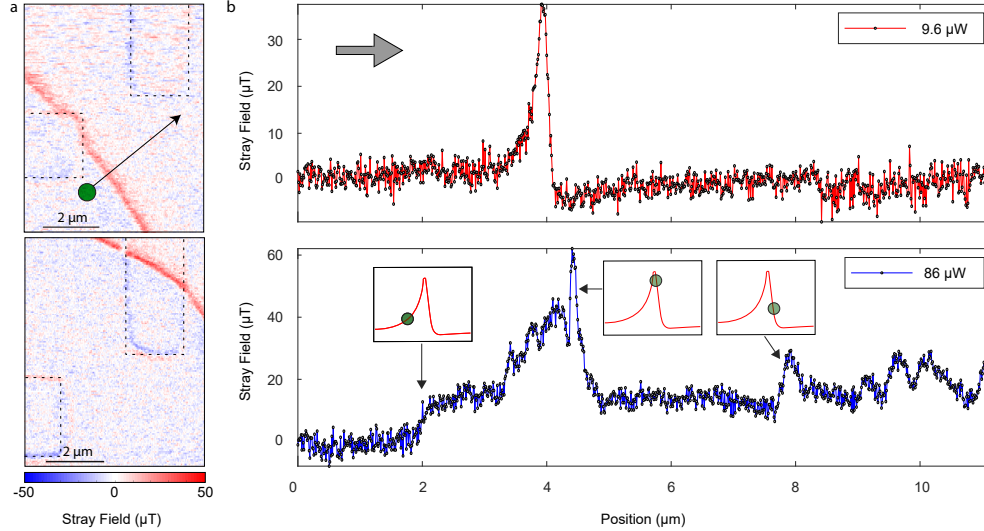
FIG. S10. **Laser dragging a** Laser dragging achieved over a large distance. The DW, originally pinned to the corner of one mesa (top) is dragged via laser in the direction shown by the black arrow. A second image (below) shows the DW becoming pinned on top of an adjacent mesa. **b** Two linescans showing NV magnetometry at low power (upper curve, red) and high power (lower curve, blue), with the powers noted in the upper right corners. The grey arrow in the top corner shows the scanning direction. In the top image, we scan across the domain wall without disturbing it, while in the bottom, we form an attractive potential, causing the domain wall to move. The insets show the relative position of the NV (green circle) to the domain wall stray field (red curve) at several positions.

[5] Rohner, D., Happacher, J., Reiser, P., Tschudin, M. A., Tallaire, A., Achard, J., Shields, B. J., and Maletinsky, P. (111)-oriented, single crystal diamond tips for nanoscale scanning probe imaging of out-of-plane magnetic fields. *Applied Physics Letters* **115**, 192401, Nov (2019).

[6] Dovzhenko, Y., Casola, F., Schlotter, S., Zhou, T. X., Büttner, F., Walsworth, R. L., Beach, G. S. D., and Yacoby, A. Magnetostatic twists in room-temperature skyrmions explored by nitrogen-vacancy center spin texture reconstruction. *Nature Communications* **9**(1), 2712 (2018).

[7] Vansteenkiste, A., Leliaert, J., Dvornik, M., Helsen, M., Garcia-Sanchez, F., and Waeyenberge, B. V. The design and verification of mumax3. *AIP Advances* **4**(10), 113007, Nov (2014).

[8] Kota, Y., Imamura, H., and Sasaki, M. Strain-induced Neel temperature enhancement in corundum-type Cr_2O_3 and Fe_2O_3. *Applied Physics Express* **6**(11), 013002 (2013).

[9] Mu, S., Wysocki, A. L., and Belashchenko, K. D. Effect of substitutional doping on the neel temperature of Cr_2O_3. *Physical Review B* **87**(5), 054435, Feb (2013).

[10] Al-Mahdawi, M., Shiokawa, Y., Pati, S. P., Ye, S., Nozaki, T., and Sahashi, M. Apparent critical behaviour of sputter-deposited magnetoelectric antiferromagnetic cr2o3 films near neel temperature. *Journal of Physics D: Applied Physics* **50**(15), 155004, Mar (2017).

[11] Foner, S. High-field antiferromagnetic resonance in Cr_2O_3. *Phys. Rev.* **130**, 183–197, Apr (1963).

[12] Hoser, A. and Koebler, U. *Renormalization Group Theory.* Springer Berlin Heidelberg, (2012).

[13] Parthasarathy, A. and Rakheja, S. Dynamics of magnetoelectric reversal of an antiferromagnetic domain. *Phys. Rev. Applied* **11**, 034051, Mar (2019).

[14] Shi, S., Wysocki, A. L., and Belashchenko, K. D. Magnetism of chromia from first-principles calculations. *Physical Review B* **79**(10), 104404, Mar (2009).

[15] Samuelsen, E., Hutchings, M., and Shirane, G. Inelastic neutron scattering investigation of spin waves and magnetic interactions in Cr_2O_3. *Physica* **48**(1), 13–42, July (1970).

[16] Mu, S. and Belashchenko, K. D. Influence of strain and chemical substitution on the magnetic anisotropy of antiferromagnetic Cr_2O_3: An ab-initio study. *Physical Review Materials* **3**(3), 034405, March (2019).

[17] Auerbach, A. *Interacting Electrons and Quantum Magnetism.* Springer New York, (1994).

[18] Ivanov, B. A. Mesoscopic antiferromagnets: statics, dynamics, and quantum tunneling (review). *Low Temperature Physics* **31**(8), 635–667 (2005).

[19] Dudko, K. L., Eremenko, V. V., and Semenenko, L. M. Magnetostriction of antiferromagnetic Cr_2O_3 in strong magnetic fields. *Physica Status Solidi (b)* **43**(2), 471–477, February (1971).

[20] Gomonay, H. V. and Loktev, V. M. Shape-induced phenomena in finite-size antiferromagnets. *Physical Review B* **75**, 174439, May (2007).

[21] Kota, Y. and Imamura, H. Narrowing of antiferromagnetic domain wall in corundum-type Cr_2O_3 by lattice strain. *Applied Physics Express* **10**(1), 013002, Dec (2016).